Wind and Structures, *Vol. 30, No. 3 (2020) 299-316*
DOI: https://doi.org/10.12989/was.2020.30.3.299

Wind pressures on a large span canopy roof

Fabio Rizzo[1a], Vincenzo Sepe[1b], Francesco Ricciardelli[2c] and Alberto Maria Avossa[*2]

[1]*Department of Engineering and Geology, University "G. d'Annunzio" di Chieti-Pescara, Pescara, Italy*
[2]*Department of Engineering, University of Campania "Luigi Vanvitelli", Aversa, Caserta, Italy*

(Received April 23, 2019, Revised November 4, 2019, Accepted January 5, 2020)

Abstract. Based on wind tunnel tests, this paper investigates the aerodynamic behavior of a large span canopy roof with elliptical plan and hyperbolic paraboloid shape. The statistics of pressure coefficients and the peak factor distributions are calculated for the top and bottom faces of the roof, and the Gaussian or non-Gaussian characteristics of the pressure time-histories in different areas of the roof are discussed. The cross-correlation of pressures at different positions on the roof, and between the top and bottom faces is also investigated. Combination factors are also evaluated to take into account the extreme values of net loads, relevant to the structural design of canopies.

Keywords: wind-induced pressures; wind tunnel tests; hyperbolic paraboloid roofs; canopy roofs; pressure coefficients; pressure correlation.

1. Introduction

Tensile roofs, made of a net of harmonic steel cables and a fabric membrane have high structural performance, with very small weight and thickness (Majowiecki 2004, Chilton 2010, Beccarelli 2015, Birchall 2015), they are efficiently used to cover large areas that need a flexible distribution of space, e.g., sports arenas.

Indeed, large canopy roofs can be subjected to rather different instantaneous wind pressure fields with respect to those acting on smaller roofs with the same shape; this is the effect of the different correlation between pressure fields on the top and bottom faces of the roof.

The hyperbolic paraboloid is the most common geometry for tensile structure; it can be obtained from two families of cables with upward and downward curvature, respectively; one bears the load and the other stabilizes the roof, depending on whether the dominating load is downward (gravity loads) or upward (wind loads).

The cables are pre-tensioned to guarantee a prescribed shape under permanent loads, and to limit the displacements under live loads. To this respect, tensile structures are highly sensitive to the dynamic effects of live loads, such as wind loads, which may cause large values of local suction and pressure (Lazzari *et al*. 2001a, 2001b, Vassilopoulou and Gantes 2010, 2011, 2012, Colliers *et al*. 2019). This is significant for canopy roofs, where the combined effect of pressures acting on the top and bottom faces may lead to large stresses, and potentially large displacements.

Limited information is available in the literature concerning the aerodynamics of hyperbolic paraboloid canopies. Uematsu *et al*. (2015) investigated the aerodynamic forces on a square plan, saddle-type canopy roof, based on the results contained in previous papers (Uematsu *et al*. 2007, 2008, and 2014) on gable, troughed and mono-sloped roofs.

Hyperbolic paraboloid roofs can have many different shapes (different floor plans, different curvatures and different heights), and the differences among them strongly affect aerodynamics and the aeroelastic behaviour (Rizzo and Sepe 2015, Rizzo and Ricciardelli 2017, Rizzo *et al*. 2018), the latter being also affected by the membrane characteristics. Letchford *et al*. (2000) and Uematsu *et al*. (2015), for example, confirm that porosity affects the pressure distributions of the roofs.

For tensile roofs, a significant role is also played by the stress state in the membrane and in load-bearing and stabilizing cables; this affects the roof stiffness and consequently the natural frequencies and damping, and therefore its dynamic behaviour. On the other hand, due to the large deformability, local and global wind loads depend on the actual (i.e., deformed) configuration of the structure. However, as shown for example by Takeda *et al*. (2014) by means of CDF analyses, pressure fields evaluated on undeformed and deformed configurations have similar trends. Therefore, the effects of deformation can be neglected in the preliminary phase of structural design, to be included only in the final design phase. Wind tunnel pressure measurements on rigid models (see e.g., Nakamura *et al*. 1994, for a similar stadium roof) are therefore the appropriate tool in the early design stage.

Notwithstanding their importance, knowledge of the aerodynamic and aeroelastic effects on hyperbolic paraboloid roofs is far from being complete, and mainly comes from numerical and wind tunnel tests performed on

[*]Corresponding author, Assistant Professor
E-mail: albertomaria.avossa@unicampania.it
[a]Assistant Professor
E-mail: fabio.rizzo@unich.it
[b]Associate Professor
E-mail: vsepe@unich.it
[c]Professor
E-mail: friccia@unicampania.it

ISSN: 1226-6116 (Print), 1598-6225 (Online)

specific structures for design purposes (e.g., Elashkar and Novak 1983, Daw and Davenport, 1989, Majowiecki 2004, Biagini *et al*. 2007, Eswaran *et al*. 2016, Ke *et al*. 2018). In addition, existing Codes give provision only for static load conditions and/or for temporary structures (e.g., CEN 2005, ASCE 2010a, ASCE 2010b, ASCE 2010c). Additional information can be found in the technical literature, such as Beccarelli (2015), or in the TensiNetDesign Guide (Foster and Mollaert, 2004), developed by the European Network for Membrane Structures "TensiNet". Comparison between results of wind tunnel tests on sample cases of hyperbolic paraboloid canopies and coefficients provided by AS-NZS 1170-2 (2011) are reported by Takeda *et al*. (2014) and Uematsu *et al*. (2014).

To contribute to fill this gap, a wind tunnel experimental campaign was performed by one of the authors, with parametric experiments on hyperbolic paraboloid models of buildings with different geometries (Rizzo and Sepe 2015, Rizzo and Ricciardelli 2017, Rizzo *et al*. 2018).

The sensitivity of tensile structures to wind-structure interaction is even more pronounced for canopies. In fact, flexible roofs of buildings are stabilized by the pneumatic stiffness of the internal volume (Lazzari *et al*. 2001a, 2001b), whereas canopies are much more flexible and their reliability closely depends on their aeroelastic behaviour.

Moreover, the aerodynamics of the bottom face of the roof can be very different from that of the top face (Natalini *et al*. 2002, 2013) and Codes give no provision for this difference and for the partial correlation between the pressure fluctuations on the top and bottom faces of the roof. These two aspects, the latter in particular, very much affect loading, therefore structural reliability.

This paper presents the results of an investigation of pressure coefficients and of their correlation within one face, and between the two faces of a hyperbolic paraboloid canopy roof. The latter aspect has been so far discussed only for other structural geometries; Ginger and Letchford (1994), for example, investigated the fluctuating pressure distributions and the cross-correlation of the area-averaged pressures on two particular roof pitches, so to estimate the total fluctuating load for a range of wind directions.

Similar structures are for example the 2000 Olympic Stadium in Sidney and the 2004 Olympic Stadium in Athens. The former was completed in March 1999 and has a 170 m x 128 m oval plan and it is composed by two fabric hyperbolic paraboloid roofs, supported by steel trusses arches. Aerodynamic and aeroelastic tests were carried out on this structure and the main results were discussed by scientific literature, as for example Holmes and Wood (2001). They describe how to obtain effective static load distributions on this roof by taking into account both the measured pressure field on rigid wind tunnel models and structural influence coefficients, according to the LRC method of Kasperski and Niemann (1992). Correlations between pressure fluctuations at different points of the roof were therefore evaluated, as a part of calculations to obtain pressure distributions corresponding to peak load effect. However, both Holmes and Wood (2001) and Kasperski and Niemann (1992) discuss the spatial correlation of wind loads on the roof and do not discuss the correlation between the top and bottom surfaces; this can have crucial effects on the local and global wind loads of canopy roofs, as it will be shown in Sections 3 to 6 below. In addition, these methods were calibrated based on Gaussian processes, while recent studies (Rizzo *et al*. 2018) have shown that for such structural shapes Gaussian processes may be not representative for large parts of the roof.

The case study reported here is based on tests performed in the CRIACIV (Inter-University Research Centre on Wind Engineering and Building Aerodynamics) boundary layer wind tunnel in Prato, Italy on the model of a project canopy of the Pescara football stadium. The paper investigates the pressure fields measured on the top and bottom faces of the roof for different wind angles.

The pressure coefficients distribution is discussed in terms of mean values, extreme values and peak factors. This is, in fact, crucial in order to estimate peak loads from experimental data, as shown in the scientific literature (Kareem 1997, Kwon and Kareem 2011, Ciampoli and Petrini 2012, Barbato *et al*. 2013).

In this paper, the correlation between pressure coefficients on the top and on the bottom is also discussed to confirm the reliability of the net peak loads given for three wind angles. As suggested by AS-NZS 1170-2 (2011), combination factors are introduced to take into account that the extreme values of net loads, relevant to the structural design of canopies, do not coincide with the algebraic difference between extreme loads on the top and on the bottom surfaces.

2. Model geometry and wind tunnel tests

Wind tunnel pressure measurements on a project canopy roof for the Pescara football stadium were performed in the CRIACIV boundary layer wind tunnel in Prato, Italy.

The roof geometry is a hollow hyperbolic paraboloid, with an elliptical plan shape for both the external and internal rings (Rizzo *et al*. 2005, D'Asdia *et al*. 2006). The design included reinforced concrete vertical structures, steel pipes (about 3 m diameter) for the main roof structure, and a cable net supporting the fiberglass roof membrane; overall plan dimensions of the roof are 251.60 m x 210.80 m, with a height of 42.50 m.

The wind tunnel used for the experiments is an open circuit, with a test chamber of 2.30 m x 1.60 m. The model (Fig. 1) was made of steel (external arches and internal ring) and Plexiglas (roof surface); wooden models of the existing sports arena and of the surrounding buildings were also built to properly reproduce aerodynamic interference.

For purpose of pressure analysis, the roof is divided into four different areas, referred to as zones A, B, C and D (Fig. 2). In particular, the three wind directions of $\theta=0°$, $\theta=45°$ and $\theta=90°$ are also shown, that will be discussed in the paper. For $\theta=0°$ the wind is parallel to the longitudinal X-X section of Fig. 1, whereas for $\theta=90°$ it is parallel to the Y-Y section of Fig. 1. Pressure measurements were taken with a sampling frequency of 252 Hz, and an acquisition time of $T_0=29.77$ s; this gave a total of 7504 time steps for each run.

To allow pressure measurement on the top and bottom

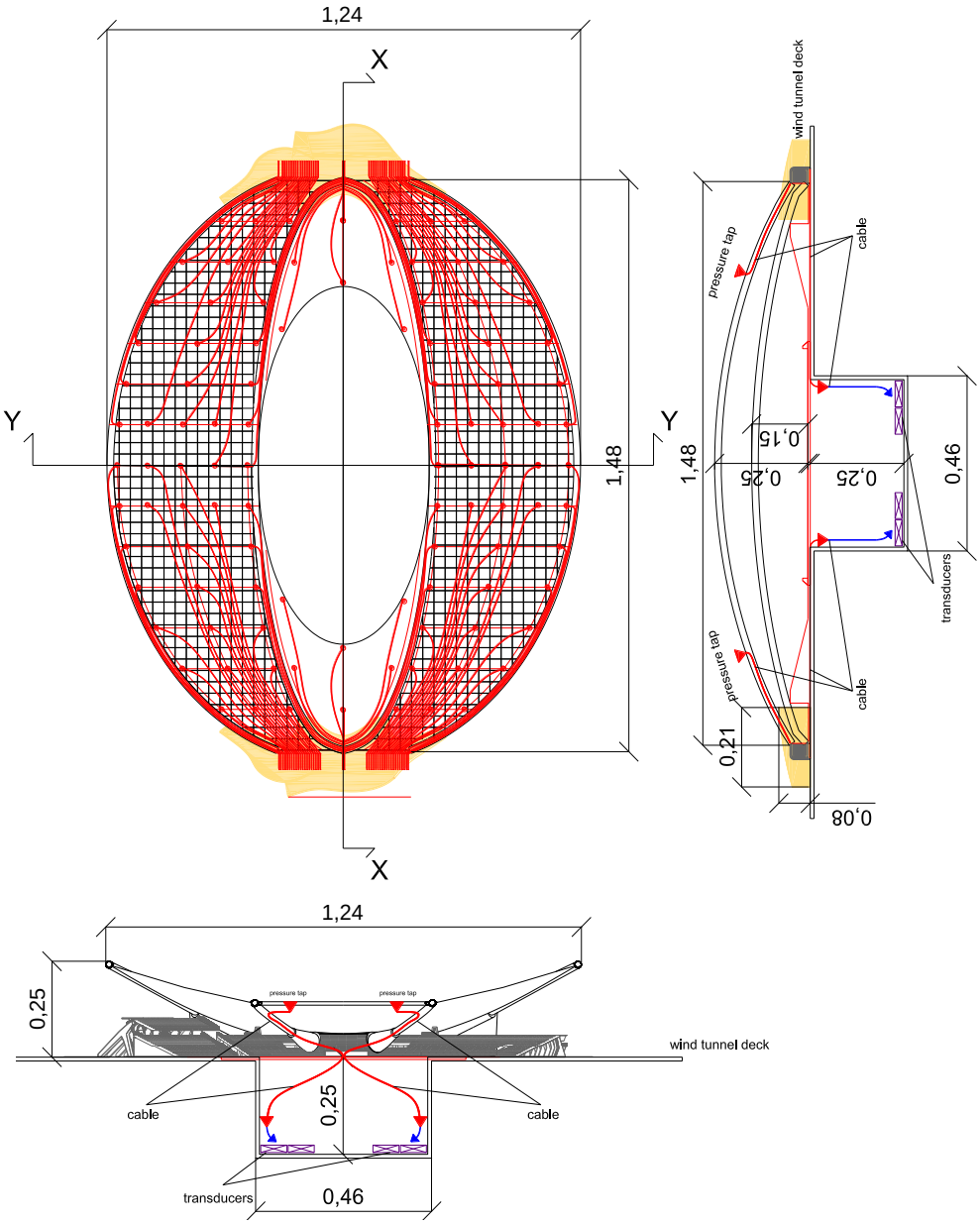

Fig. 1 Wind tunnel model: roof plan section X-X and section Y-Y; dimensions in metres

faces of the canopy, a minimum roof thickness of 5 mm was required. A geometric scale of 1:170 was chosen for the model (Fig. 3(a)), which brought plan dimensions of 1.48 m x 1.24 m, and a maximum height of 0.27 m; this allowed accommodating 90 + 90 pressure taps on the top and bottom faces of the canopy, respectively. There resulted a blockage of 8% to 12% if the rectangular envelope of the model is considered, depending on the angle of attack; this reduces to less than 6% if the actual projected area of the model is considered. This required correction of the measured pressures, according to Sahini (2004).

Measurements were taken for sixteen angles of attack, but only the results for 0°, 45°, and 90° are discussed in the following.

Fig. 3(b) shows the velocity and turbulence intensity profiles as measured in the wind tunnel, corresponding to a category III exposure with z_o=0.247(Rizzo and Ricciardelli, 2017). In the range of heights where the roof was located (10 to 27 cm from the tunnel floor) the mean wind speed ranged between 17 to 21 m/s, and the turbulence intensity between 10% and 15%.

The 180 pressure taps were connected to pressure scanners (sections XX, YY in Fig. 1) via copper tubes with an internal diameter of 1.5 mm, which brought a flat frequency response up to 100 Hz.

The aerodynamic shape of the arches (i.e. circular cross section) requires a careful scaling of their roughness, that for the prototype is due to steel plates and other elements welded or connected by bolts. Taking into account the geometrical scaling, a roughness size of 0.1 mm (i.e., 0.02 m full scale) was reproduced on the arches of the model.

Pressure tap numbering (Fig. 2) refers to plan location; therefore each number corresponds to two taps, located on the top and bottom faces, respectively.

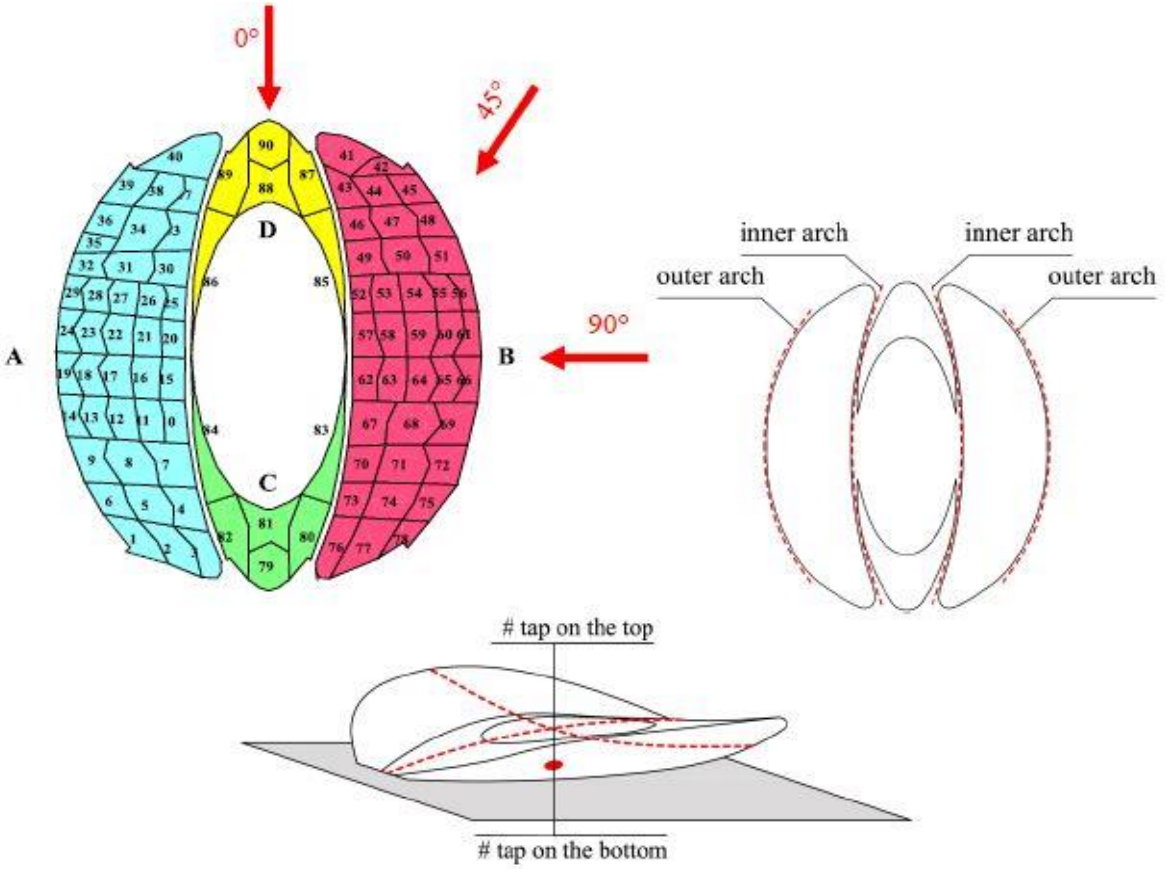

Fig. 2 Pressure tap location and areas of the roof

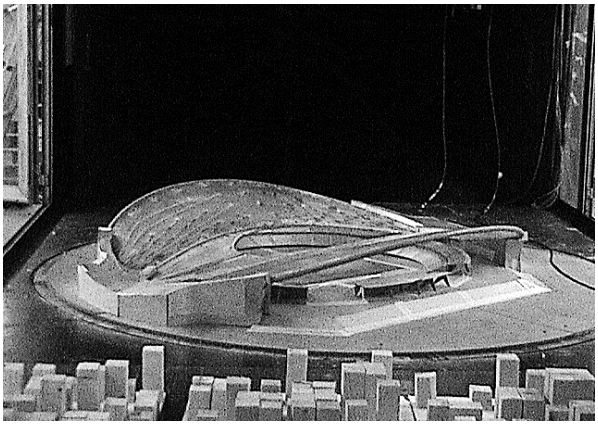

(a) Model

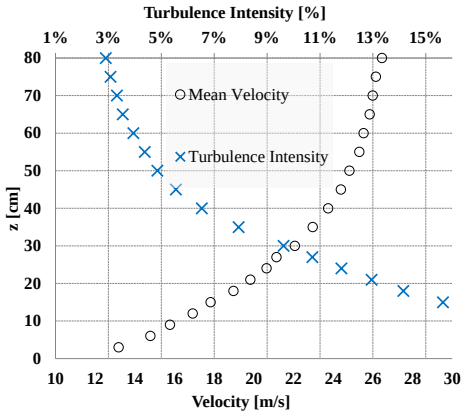

(b) Velocity and turbulence intensity profiles

Fig. 3 Wind tunnel test setup

3. Mean, maximum and minimum pressure distributions

The statistics of the pressure coefficients were analyzed, as follows

$$c_p(P,t) = \frac{p(P,t) - p_0}{\frac{1}{2}\rho V_m^2} \quad (1)$$

where $p(P,t)$ is the measured pressure at point P of the roof surface, p_0 is the static pressure in the bare tunnel and $\frac{1}{2}\rho V^2_m$ is the dynamic pressure measured by a pitot located above the model and outside the boundary layer.

In particular, the pressures acting on the top and bottom faces of the roof were considered, together with the net pressures, as defined and shown in Fig. 4, for the three wind angles θ of 0°, 45° and 90° (Fig. 2).

For each angle, maximum, minimum and mean top, bottom and net pressure coefficients are discussed. Maximum and minimum pressure coefficients have

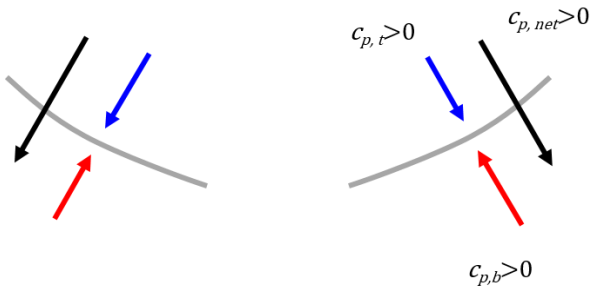

Fig. 4 Definition of pressure and net pressure coefficients

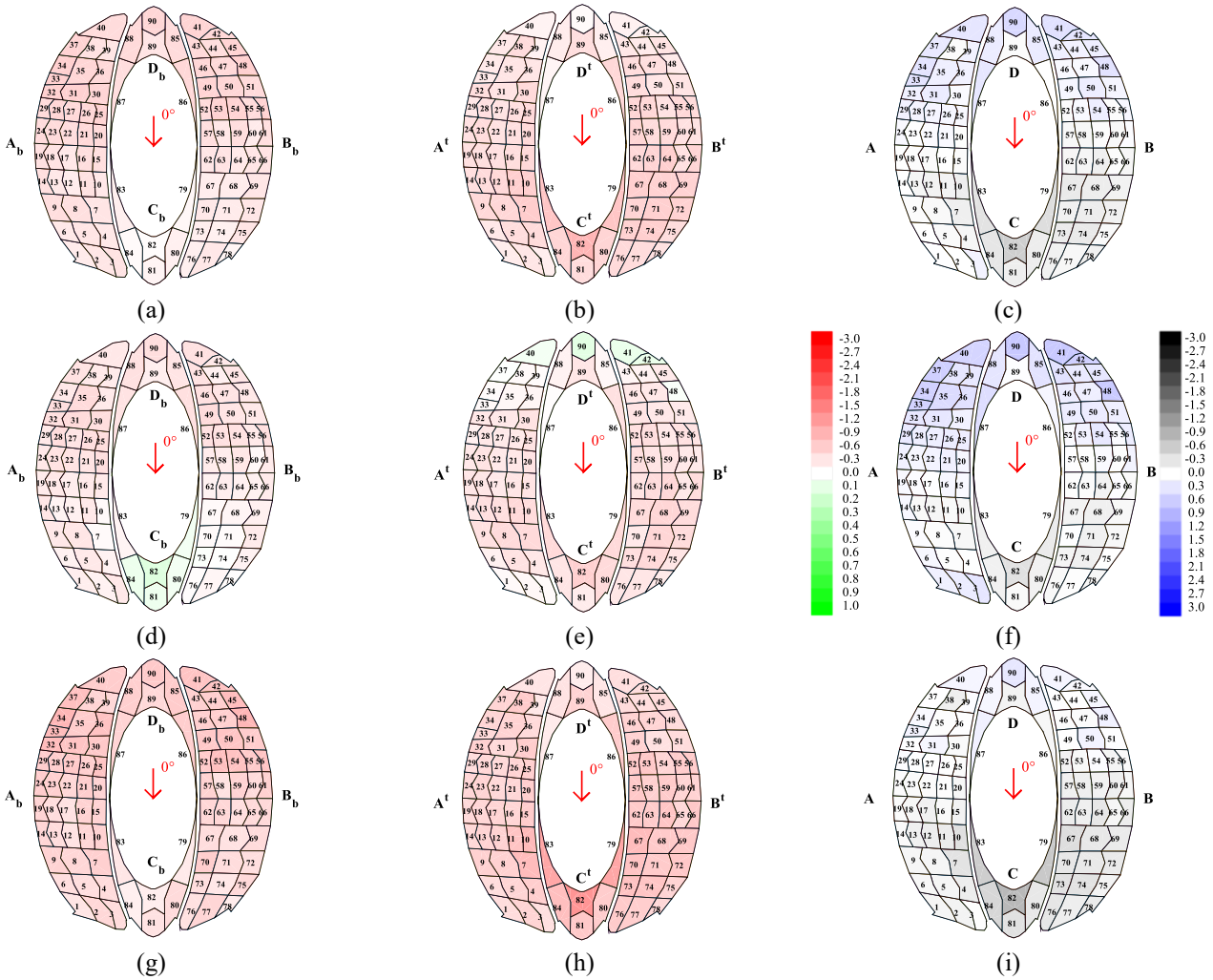

Fig. 5 Pressure coefficients for θ=0°: (a) $C_{p,m}$bottom, (b) $C_{p,m}$top, (c) $C_{p,m}$net, (d) $C_{p,max}$bottom, (e) $C_{p,max}$top, (f) $C_{p,max}$net, (g) $C_{p,min}$bottom, (h) $C_{p,min}$top, (i) $C_{p,min}$net

been obtained following the procedure of Cook and Mayne (1979, 1980); these are the pressure coefficients that combined with the 10-minute average, 50-year return period wind speed give rise to the 50-year return period maximum and minimum pressures, respectively.

3.1 Pressure coefficients for a wind angle θ=0°

For θ=0° Fig. 5 shows mean, maximum and minimum values for bottom, top and net pressure coefficients. For this angle of attack, the flow is parallel to the longitudinal section X-X in Fig. 1 and to the roof downward curvature.

Figs. 5(a)-5(c) show the mean values of bottom, top and net pressure coefficients, respectively. The mean pressure coefficients are negative almost everywhere on the roof, both on the bottom and top faces. On the bottom face they range between -0.50 and 0.02, whereas on the top face they are between -0.78 and 0.05. Net pressure coefficient values

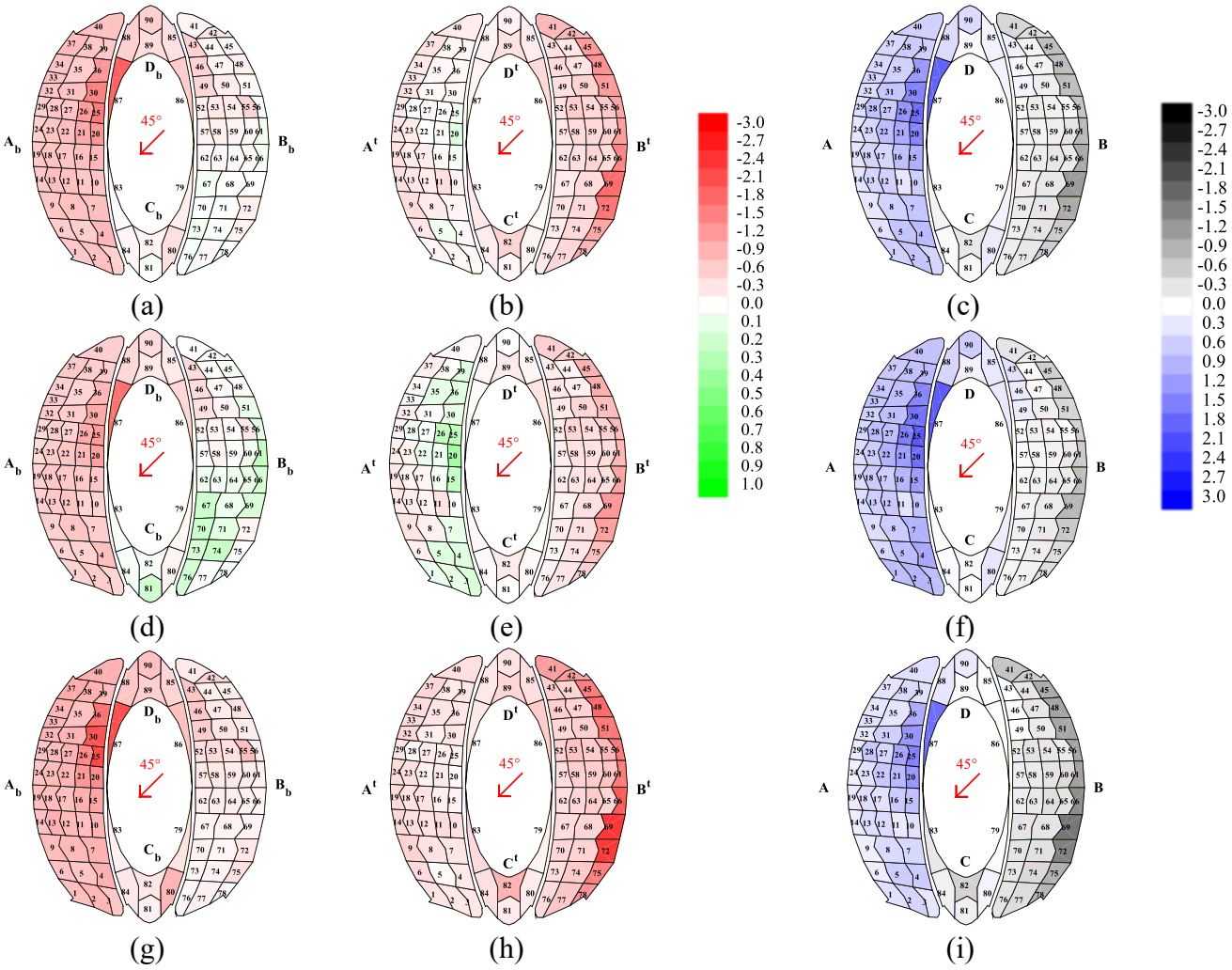

Fig. 6 Pressure coefficients for θ=45°, (a) $C_{p,m}$bottom, (b) $C_{p,m}$top, (c) $C_{p,m}$net, (d) $C_{p,max}$bottom, (e) $C_{p,max}$top, (f) $C_{p,max}$net, (g) $C_{p,min}$bottom, (h) $C_{p,min}$top, (i) $C_{p,min}$net

are between -0.75 and 0.45, with positive values being the effect of larger negative pressures on the bottom face combined with smaller negative values or positive values on the top face. The largest suctions on the bottom face (Fig. 5(a)) are located in the flow detachment zones (i.e., zone D and the upwind portions of zones A and B), whereas the smallest values occur in zone C. Contrarily, the largest values of suction on the top face (Fig. 5(b)) occur in zone C and the smallest in zone D. As a result, the largest negative net pressures occur in zone C and the largest positive pressure coefficients occur in zone D, as shown in Fig. 5(c). It must be noticed, that here and in the following some asymmetries of the coefficients in symmetric configurations are found; besides experimental deviations, these can be ascribed to the non-symmetric distribution of the pressure taps and to non-symmetric arrangement of the surrounding buildings.

The maximum pressure coefficients maps shown in Figs. 5(d) and 5(e) and the minimum pressure coefficients maps shown in Figs. 5(g) and 5(h), for the bottom and top surface, respectively, are consistent with the observations made about the mean pressure coefficients. The largest positive values of the maximum pressure coefficient are in the order of 0.12, and are located in zone C for the bottom face and in zone D and on the upwind portion of zones A and B for the top face, respectively (Figs. 5(d) and 5(e)). For the rest of the roof, maximum pressures are negative, on both the bottom and top faces. Minimum pressures are negative everywhere, both on the bottom and top faces (Figs. 5(g) and 5(h)); the largest minimum pressure coefficients are in the order of -1.12, and are located in zone D for the bottom face and in zone C for the top face, respectively.

The maximum and minimum net pressure coefficients are shown in Figs. 5(f)-5(i). The largest maximum net pressure coefficients are in the order of 0.53, and are located in zone D, and in the upwind portions of zones A and B; the largest minimum net pressure coefficients are in the order of -1.09, and are located in zone C.

Globally, for θ=0° the flow streamlines follow the roof curvature and the structure shape minimizes the wind action. Net pressures decrease in an almost linear fashion from the leading edge to the trailing edge of the roof. In addition, and differently from the other cases that will be discussed below, the pressure coefficients show a smooth variation across the different zones of the roof, without abrupt sign reversals.

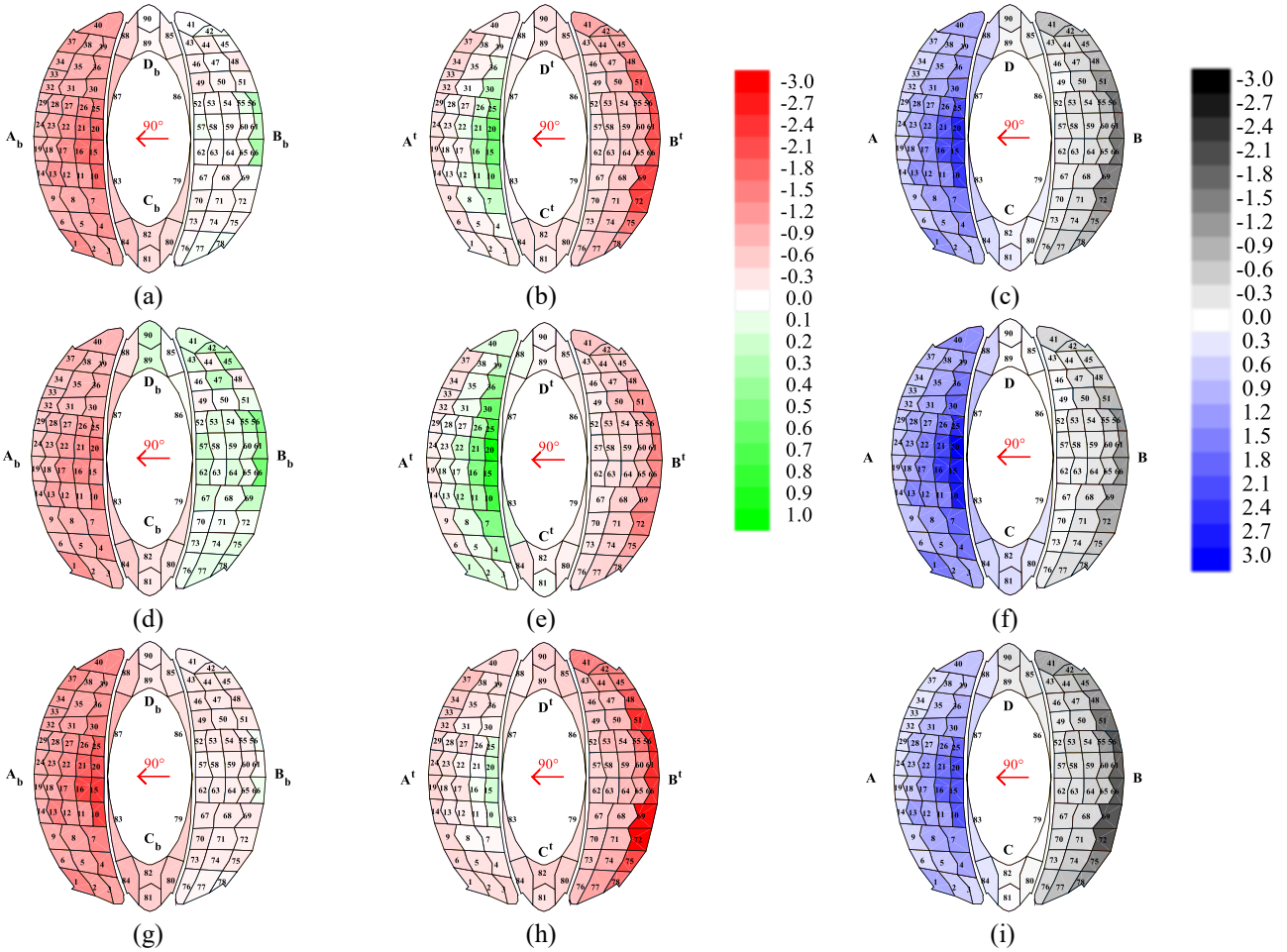

Fig. 7 Pressure coefficients for θ = 90°: (a) $C_{p,m}$bottom, (b) $C_{p,m}$top, (c) $C_{p,m}$net, (d) $C_{p,max}$bottom, (e) $C_{p,max}$top, (f) $C_{p,max}$net, (g) $C_{p,min}$bottom, (h) $C_{p,min}$top, (i) $C_{p,min}$net

This indicates that for a wind angle θ=0° the cable net is not prone to instability phenomena, typically caused by load patterns with changing sign.

3.2 Pressure coefficients for a wind angle θ=45°

Fig. 6 shows the mean, maximum, minimum values for bottom, top and net pressure coefficients, for the wind angle θ=45°. Like for θ=0°, the pressure distribution is dominated by suctions, the largest values of which on the bottom face correspond to the smallest values on the top face, and vice versa. In particular, suctions dominate the pressure distribution on the bottom face of zone A and on the top face of zone B.

Figs. 6(a) and 6(b) show the mean pressure coefficients on the bottom and on the top faces, respectively. The maximum suction on the bottom face (Fig. 6(a)) occurs in the lower, upwind portion of zone A and in zone D, and the minimum pressure coefficient is -1.68; in the same area there are also the maximum pressures on the top face, with a maximum pressure coefficient of 0.11 at pressure tap #20 (Fig. 6(b)). Similarly, the maximum suction on the top face (Fig. 6(b)) occurs in the upper, downwind portion of zone B, and the minimum pressure coefficient is -1.56; in the same area there are also the maximum pressures on the bottom face, with a maximum pressure coefficient of 0.05 at pressure tap #57 (Fig. 6(a)). Mean net pressure coefficients shown in Fig. 6(c) summarize what has been observed for the two faces separately; indeed, zone A is acted upon by positive, downward mean net pressures (maximum mean net pressure coefficient is 1.55), whereas zone B is acted upon by negative, upward, mean net pressures (minimum mean net pressure coefficient is -1.56).

Positive maximum pressures occur only in zone B for the bottom face (Fig. 6(d)) and in zones A and C for the top face (Fig. 6(e)); for the rest of the roof maximum pressures are negative. The maximum pressure coefficient never exceeds 0.22 on the bottom face, and 0.35 on the top face. The minimum pressures are negative on both faces all over the roof. The minimum values occur at the lower, upwind portion of zone A and in zone D for the bottom face (Fig. 6(g)), and at the upper, downwind portion of zone B for the top face (Fig. 6(h)); the lowest values of the minimum pressure coefficient are -1.98 and -2.12, respectively. The

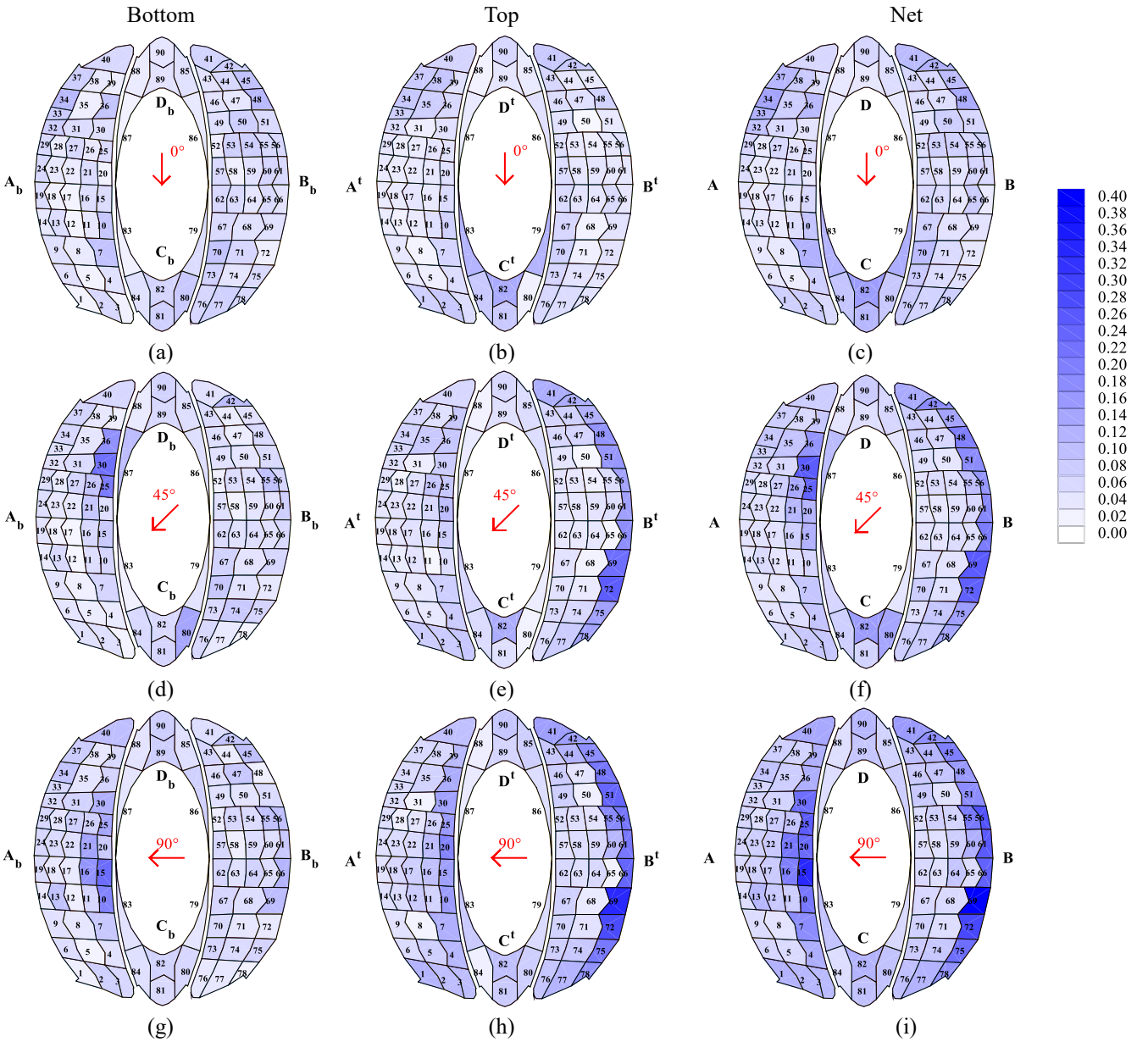

Fig. 8 Standard deviation: (a) σ_{Cp}bottom, (b) σ_{Cp}top, (c) σ_{Cp}net for θ=0° ; (d) σ_{Cp}bottom, (e) σ_{Cp}top, (f) σ_{Cp}net for θ=45; (g) σ_{Cp}bottom, (h) σ_{Cp}top, (i) σ_{Cp}net for θ=90°

maps of the maximum and minimum net pressure coefficients show the same pattern as that of the mean net pressure coefficient, with positive, downward net pressures in zone A and negative, upward, net pressures in zone B. The maximum and minimum net pressure coefficients are 1.67 and -2.13, respectively.

3.3 Pressure coefficients for a wind angle θ=90°

For θ=90° Fig. 7 shows mean, maximum and minimum values for bottom, top and net pressure coefficients. For this angle of attack, the flow is parallel to the longitudinal section Y-Y in Fig. 1 and to the roof upward curvature.

Figs. 7(a)-7(c) show the mean values of bottom, top and net pressure coefficients, respectively. The mean pressure coefficients are negative on the bottom faces of zones A, C and D, and on the top faces of zones B, C and D. On the bottom face of zone B, mean pressures vary from moderately negative to moderately positive, whereas on the top face of zone A they also change sign, but positive values are much larger. On the bottom face, pressure coefficients range between -1.61 and 0.31, whereas on the top face they are between -2.01 and 0.58. As combination of pressures on the two faces, net pressures (Fig. 7(c)) are positive in zone A, negative in zone B and of both signs in zones C and D. Net pressure coefficients are between 0.30 and 2.17 in zone A and between -2.18 and -0.3 in zone B.

The maximum and minimum pressure distributions replicate those of the mean pressures. The largest positive values of the maximum pressure coefficient on the bottom face are in the order of 0.31, and are located in pressure tap #66, zone B (Fig. 7(d)). The largest positive values of the

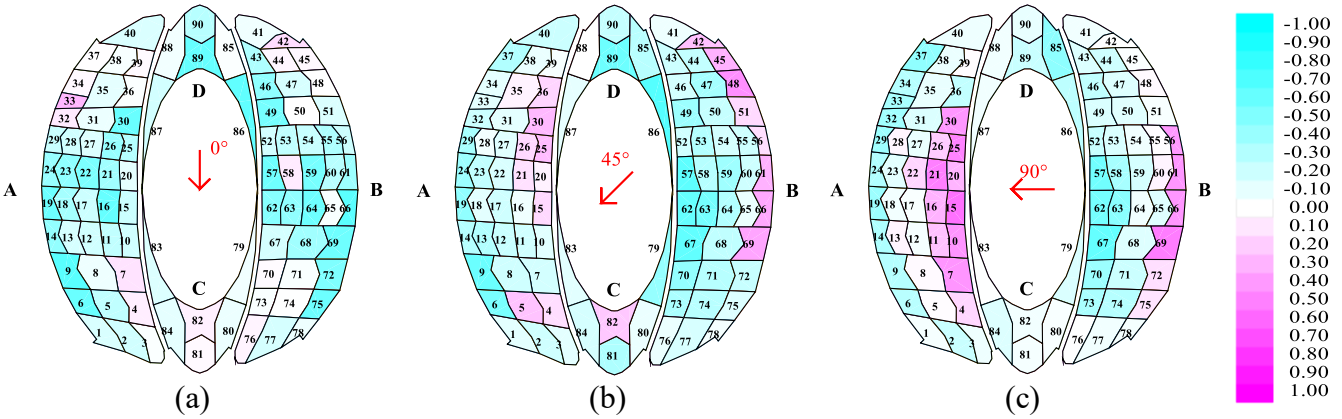

(a) (b) (c)

Fig. 9 Correlation coefficient between pressure fluctuation on the top and bottom faces for wind angles of θ=0°(a), θ=45° (b) and θ=90° (c)

maximum pressure coefficient on the top face are in the order of 0.57, and are located in the pressure tap #20, zone A (Fig. 7(e)). The bottom face of zone A and the top face of zone B feature negative maximum pressures. Minimum pressures are negative everywhere, except for a limited area in the internal and middle upwind portion of the top face of zone A. The largest minimum pressure coefficients are in the order of -2.12 for the bottom face (Fig. 7(g)) and in the order of -2.70 for the top face (Fig. 7(h)); in both cases, the largest suctions occur around the leading edge of the roof, where separation occurs.

Also in this case, the maps of the maximum and minimum net pressure coefficients show the same pattern as that of the mean net pressure coefficient, with positive, downward net pressures in zone A and negative, upward, net pressures in zone B. The maximum and minimum net pressure coefficients are 2.54 and -2.67, respectively.

4. Pressure fluctuations and their spatial correlation

Fig. 8 shows the distributions of the Standard Deviation (STD) of the pressures coefficients on the bottom and top faces and of the net pressure coefficients, for the three wind angles considered.

In general, it is observed that on both faces the largest pressure fluctuations correspond to the largest mean pressures, in particular with the largest suctions. The STD of the pressure coefficients for a wind angle θ=0° are given in Fig. 8(a) for the bottom face and in Fig. 8(b) for the top face; the values are rather uniform, and range between 0.02 and 0.10. The STD of the pressure coefficients for a wind angle θ=45° are given in Fig. 8(d) for the bottom face and in Fig. 8(e) for the top face; the values are more variable, and range between 0.02 and 0.18. Finally, the STD of the pressure coefficients for a wind angle θ=90° are given in Fig. 8(g) for the bottom face and in Fig. 8(h) for the top face, with values ranging between 0.01 and 0.34.

In Figs. 8(c), 8(f) and 8(i), the STD of the net pressure coefficients are shown. Large net pressure fluctuations are the effects not only of large pressure fluctuations on the two faces, but also of a high correlation of these. In fact, large but uncorrelated pressure fluctuations on the two faces give rise to moderately large net pressure fluctuations, and negatively correlated large pressure fluctuations on the two faces give rise to small net pressure fluctuations, as the pressure fluctuations on the two sides tend to cancel with each other. This effect is clearly visible for a wind angle θ=90°, for which moderate pressure fluctuations on the two sides of the upwind edge of zone A give rise to large net pressure fluctuations, due to the large positive correlation.

For a better understanding of this issue, the correlation between the pressure coefficients on the bottom and upper faces was investigated. The correlation coefficient between the pressure fluctuations at the *i*–th pressure tap on the bottom and top faces is defined as

$$R_i = -\frac{cov\left[C_{p,i}^{b}, C_{p,i}^{t}\right]}{\mathrm{STD}\left[C_{p,i}^{b}\right] \cdot \mathrm{STD}\left[C_{p,i}^{t}\right]} \tag{2}$$

where $C_{p,i}^{b}$ and $C_{p,i}^{t}$ denote the pressure coefficient at the *i*–th pressure tap on the bottom and top faces, respectively. The minus sign in Eq. (2) brings a positive correlation when top and bottom pressures combine in an unfavorable way, so to give rise to large net pressures. In particular, Fig. 9 shows the correlation coefficients distribution for θ equal to 0°, 45° and 90°, between the same pressure taps on the bottom and top faces.

For θ=0° (Fig. 9(a)) the pressure correlation coefficient R_i ranges between -0.65 at pressure tap #9 and 0.28 at pressure tap #33; for θ=45° (Fig. 9(b)) it ranges between -0.67 at pressure tap #86 and 0.44 at pressure tap #48; for θ=90° (Fig. 9(c)) it ranges between -0.60 at pressure tap #67 and 0.56 at pressure tap #15. It is observed that top and bottom pressures mainly combine in a favorable way, therefore giving rise to net pressure fluctuations lower than the sum of the pressure fluctuations on the two sides. Only in areas were violent flow separation takes place the correlation is positive and the pressures on the two sides combine in an unfavorable way.

The two different types of combination between top and bottom pressures is illustrated through Fig. 10. In particular, Fig.10(a) shows 10 minutes full scale of the time series of bottom, top and net pressure coefficients at tap #15 for

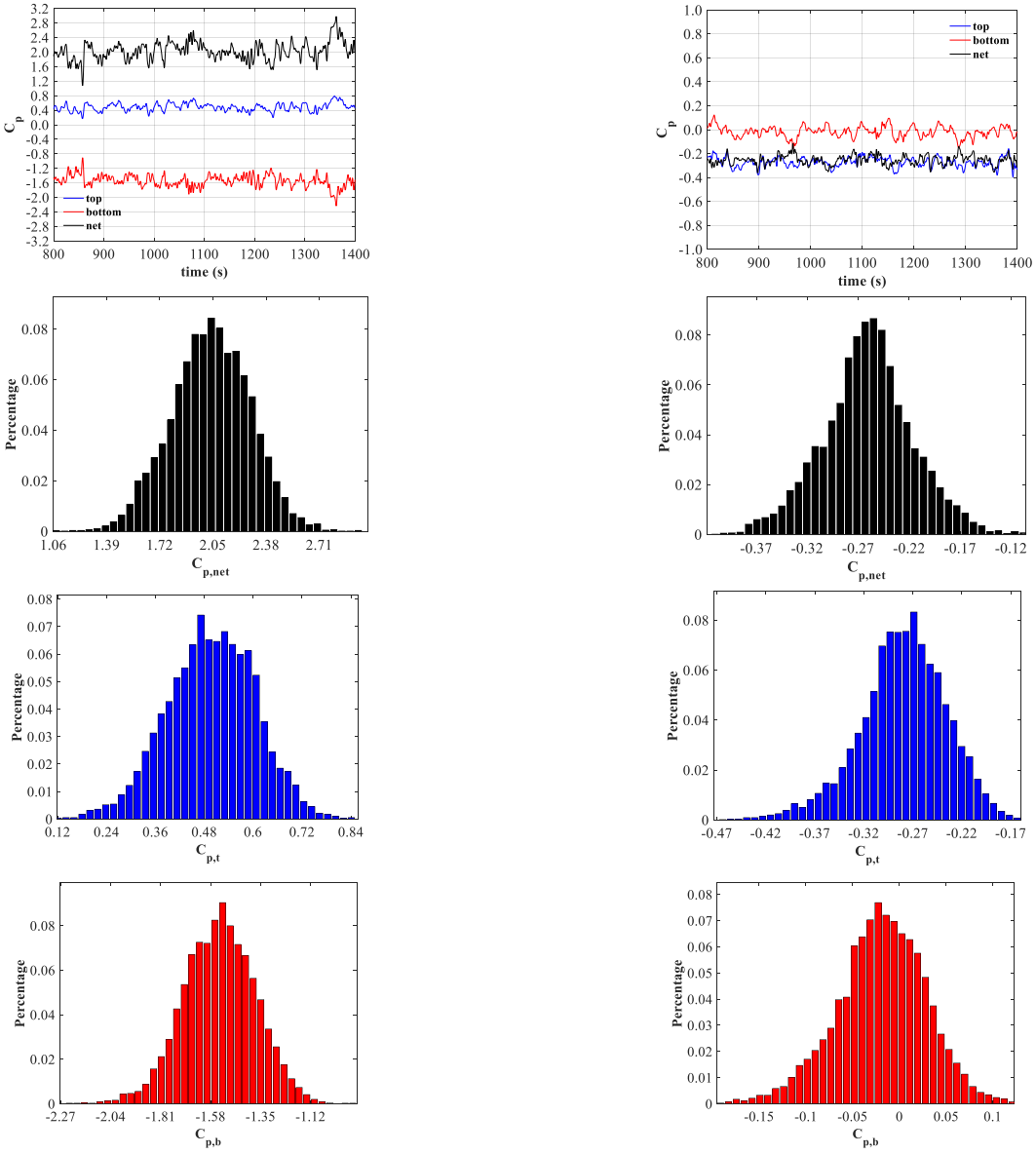

(a) (b)

Fig. 10 Sample time histories and probability density functions of the pressure coefficients at pressure taps #15 (a) and # 57 (b) for θ=90°

θ=90°, together with their PDFs. A large mean net pressure is the combination of a positive mean pressure on the top face with a negative mean pressure on the bottom face; pressure fluctuations on the top and bottom faces also combine in an unfavorable way, so to give rise to large net pressure fluctuations.

Fig. 10(b) shows the same time series and PDFs for tap #57; in this case the mean pressure on the bottom face is very low, and the mean net pressure almost coincides with the mean pressure on the top face; pressure fluctuations on the two faces are low, and negatively correlated, which gives rise to moderate net pressure fluctuations.

5. Pressure series probability distribution

According to Suresh Kumar and Stathopoulos (2000) the roof regions where pressure coefficients are non–Gaussian processes are identified by $|\gamma_{cp}|>0.5$ and/or $|k_{cp}|>0.5$, where γ_{cp} is the skewness and k_{cp} is the excessive kurtosis of the process (Rizzo *et al*. 2018).

Table 1 summarizes the skewness and excessive kurtosis maximum, minimum and mean values for θ=0°, 45° and 90° and for all the pressure taps of the bottom and top faces of the roof. Skewness is mainly moderately negative, with mean values ranging between -0.138 and -0.236; positive values exist, up to 1.1, while negative values can be as low as -1.839, indicating a longer left tail of the distribution, and therefore potentially higher peak factors. It is also observed that the values of skewness are quite similar between the bottom and top faces. Excessive kurtosis shows a much larger variation; the mean value is always positive; negative values exceed -0.5, and positive values can be as large as

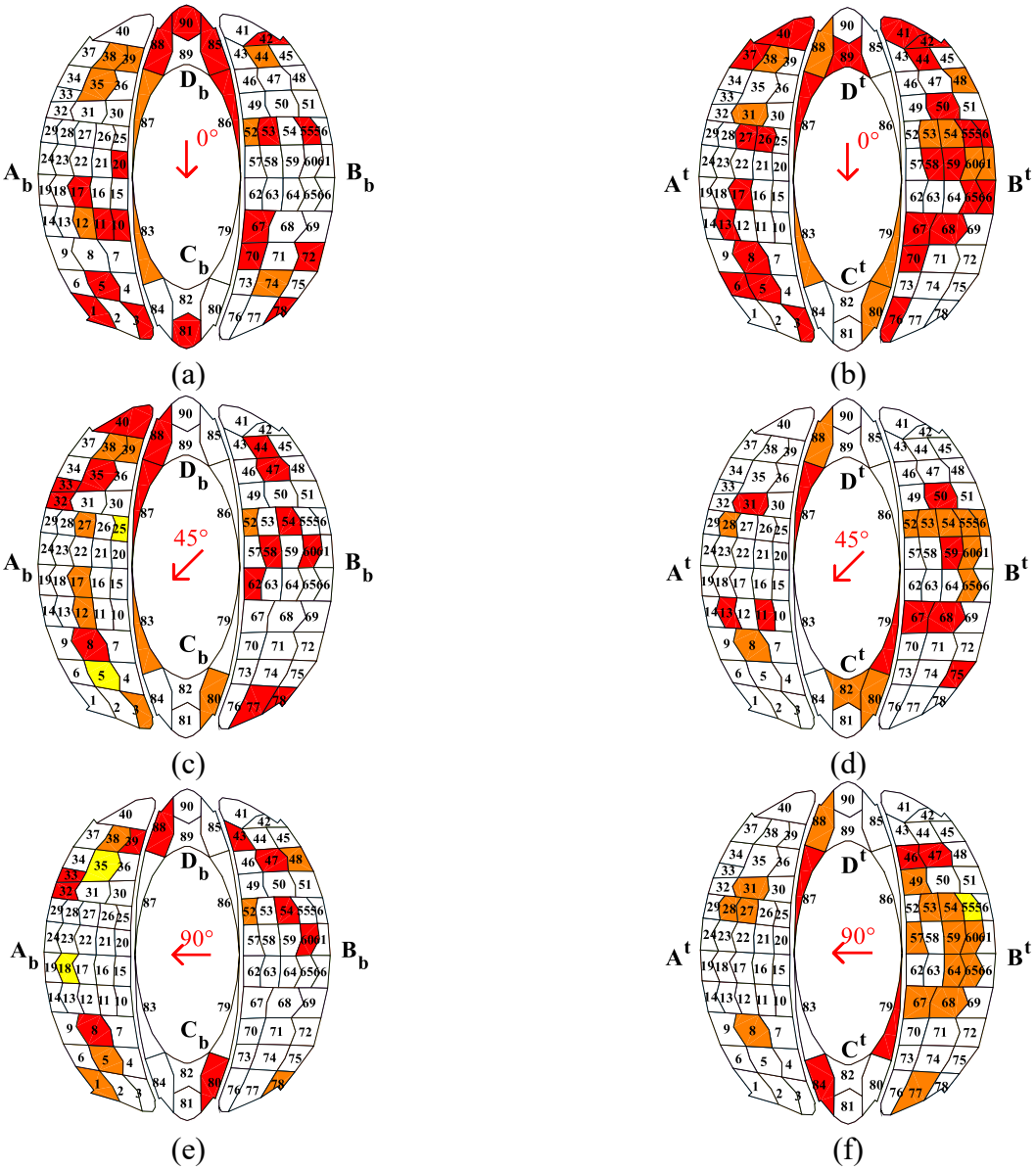

Fig. 11 Gaussian and non-Gaussian processes for θ=0°, on the bottom (a) and on the top (b) faces; for θ=45°, on the bo ttom (c) and on the top (d) faces; for θ=90°, on the bottom (e) and on the top (f) faces. Yellow areas correspond to $|\gamma_{cp}|>0.5$; red areas correspond to $|k_{cp}|>0.5$; orange areas correspond to $|\gamma_{cp}|>0.5$ and $|k_{cp}|>0.5$; white areas correspond to Gaussian behavior

Table 1 Skewness and excessive kurtosis of pressure coefficients

		0°			45°			90°		
		max	min	mean	max	min	mean	max	min	mean
γ_{cp}	top	0.843	-1.377	-0.138	0.796	-1.126	-0.182	0.384	-1.824	-0.236
	bottom	1.080	-1.838	-0.182	0.431	-1.839	-0.229	0.394	-1.701	-0.165
k_{cp}	top	6.609	-0.972	0.541	5.116	-0.304	0.468	17.93	-0.286	0.689
	bottom	13.71	-1.164	0.711	9.700	-0.622	0.736	9.121	-0.493	0.437

17.93, indicating the existence of very narrow PDFs.

The values of skewness and kurtosis suggest that a significant number of pressure coefficients have a non-Gaussian behavior. Fig. 11 shows the pressure taps at which pressure fluctuations can be considered as non-Gaussian, according to the criterion of Suresh Kumar and Stathopoulos, on the bottom and top faces, respectively, and for wind angles of 0°, 45° and 90°. In Fig. 11 yellow areas indicate that $|\gamma_{cp}|>0.5$, red areas indicate that $|k_{cp}|>0.5$, and orange areas indicate that both $|\gamma_{cp}|>0.5$ and $|k_{cp}|>0.5$; white areas correspond to a Gaussian behavior.

Comparison of Fig. 11 with Figs. 5 - 8 suggests that

Table 2 Extension of the areas on the roof featuring non-Gaussian pressures

			Zones				
	Wind-Angle		A	B	C	D	$\sum S_t$
Bottom	0°	S_z	33%	48%	45%	59%	
		S_t	13%	19%	4%	6%	42%
	45°	S_z	12%	30%	55%	37%	
		S_t	5%	12%	5%	4%	26%
	90°	S_z	10%	34%	37%	37%	
		S_t	4%	14%	4%	4%	26%
Top	0°	S_z	28%	29%	32%	82%	
		S_t	11%	11%	3%	8%	33%
	45°	S_z	33%	22%	32%	37%	
		S_t	13%	9%	3%	4%	29%
	90°	S_z	22%	16%	23%	23%	
		S_t	9%	7%	2%	2%	20%

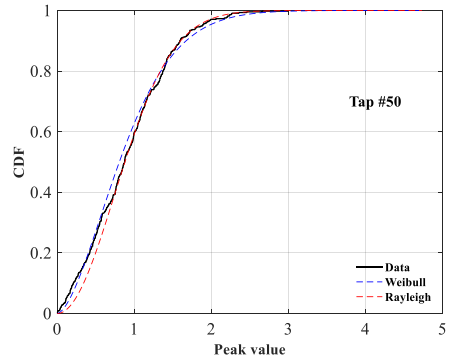

(a) Bottom

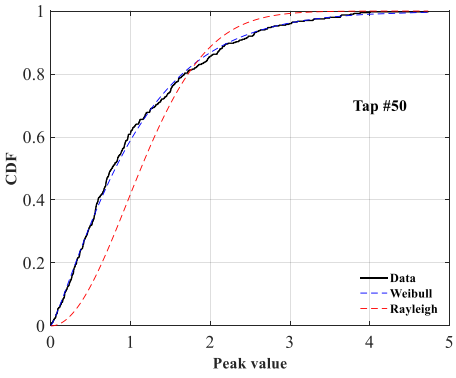

(b) Top

Fig. 12 CDF of the absolute value of pressure coefficient peaks: (a) at pressure tap #50 for θ=45°, on the bottom face, (Gaussian case), (b) at pressure tap #50 for θ=45°, on the top face, (non-Gaussian case)

there exists no evident relationship between the mean and fluctuating pressure coefficients on one side, and the Gaussian or non-Gaussian behavior of the pressure on the other side.

Two examples of the Cumulative Distribution Function (CDF) of the absolute value of local peaks are shown in Fig. 12, featuring Gaussian (Fig. 12(a)) and non-Gaussian (Fig. 12(b)) behaviour, respectively. The former is well described through a Rayleigh distribution, whereas the latter requires a two-parameter Weibull distribution (Davenport 1964, Huang *et al.* 2013). Results obtained by a one-sample Kolmogorov-Smirnov test (Massey 1951) also confirm this difference.

In Table 2, the extension of the areas on the roof featuring non-Gaussian pressures, is shown. This is given by two ratios: $S_z = S_{nG}/S_{zone}$ and $S_t = S_{nG}/S_{tot}$, where S_{nG} is the area of the roof featuring non-Gaussian pressures, S_{zone} are the areas of zones A, B, C and D, respectively, and S_{tot} is the total area of the roof.

Table 2 shows moderate differences between bottom and top faces, and between the different angles of attack. On average one-third of the areas is subjected to non-Gaussian pressure distributions, with a slightly larger value for the bottom face and a slightly lower value for the top surface. It is also observed that larger areas exposed to non-Gaussian pressures are found for θ=0°, where the flow stays more attached to the roof, and smaller areas exposed to non-Gaussian pressures are found for θ=90°, where the strongest separation occurs.

5. Pressure peak factors

Peak factors are crucial in the evaluation of peak loads (Kwon and Kareem 2011), and for canopy roofs they may determine a stable or unstable behavior. In addition, modern performance-based reliability design approaches require the accurate estimation of extreme wind loads and their distribution (Ciampoli and Petrini 2012, Barbato *et al.* 2013, Giaralis and Petrini 2017, Rizzo *et al.* 2018).

Peak factors are defined according to Eq. 3. They are obtained from both, maximum (g_{max}) and minimum (g_{min}) pressure coefficients, as follows

$$C_{p,max} = C_{p,m} + g_{max}\ \sigma_{C_p}$$
$$C_{p,min} = C_{p,m} - g_{min}\ \sigma_{C_p} \quad (3)$$

where, $C_{p,m}$ and σ_{Cp} are the mean and the standard deviation of the pressure coefficients time history, recorded by each pressure tap; the maxima $C_{p,max}$ or minima $C_{p,min}$ pressure coefficients are estimated according to Cook and Mayne (1979, 1980).

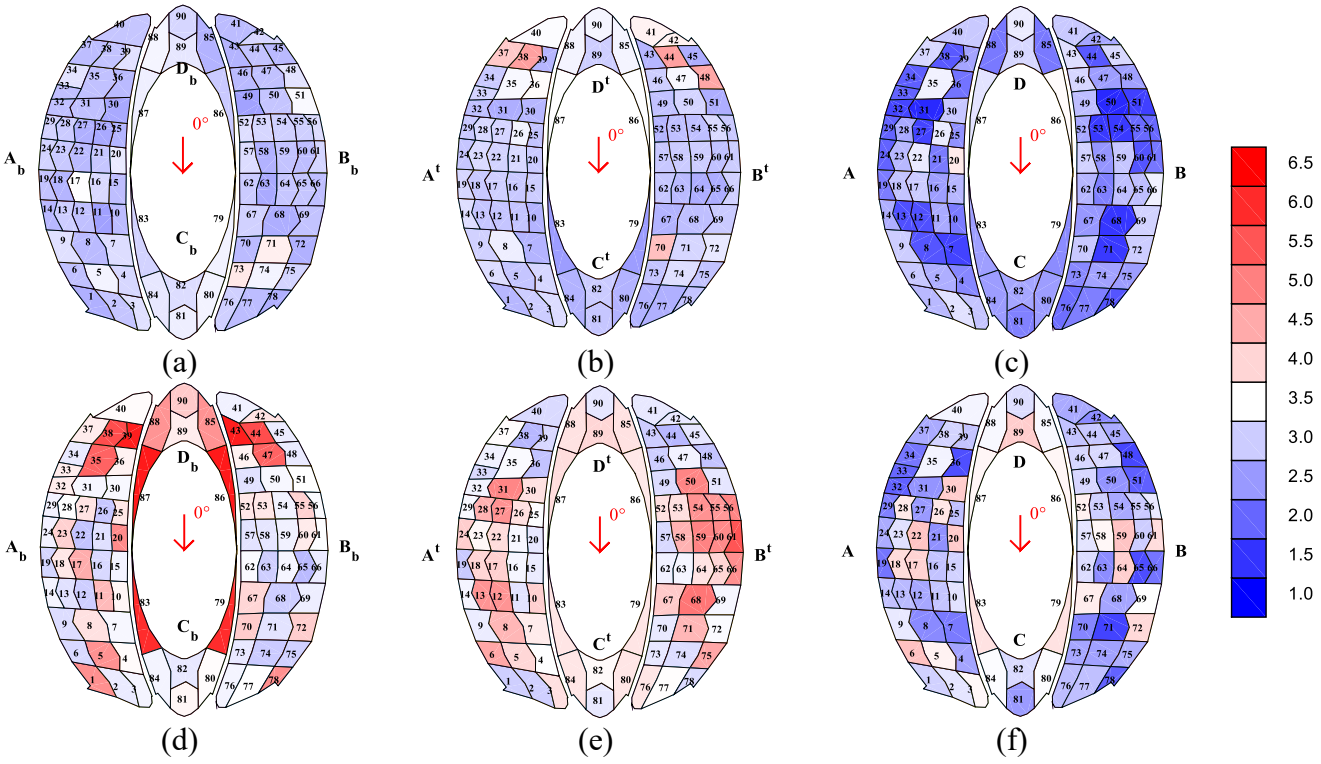

Fig. 13 Peak factors: (a) $g_{,max}$bottom, (b) $g_{,max}$top, (c) $g_{,max}$net, (d) $g_{,min}$bottom, (e) $g_{,min}$top, (f) $g_{,min}$net, θ=0°

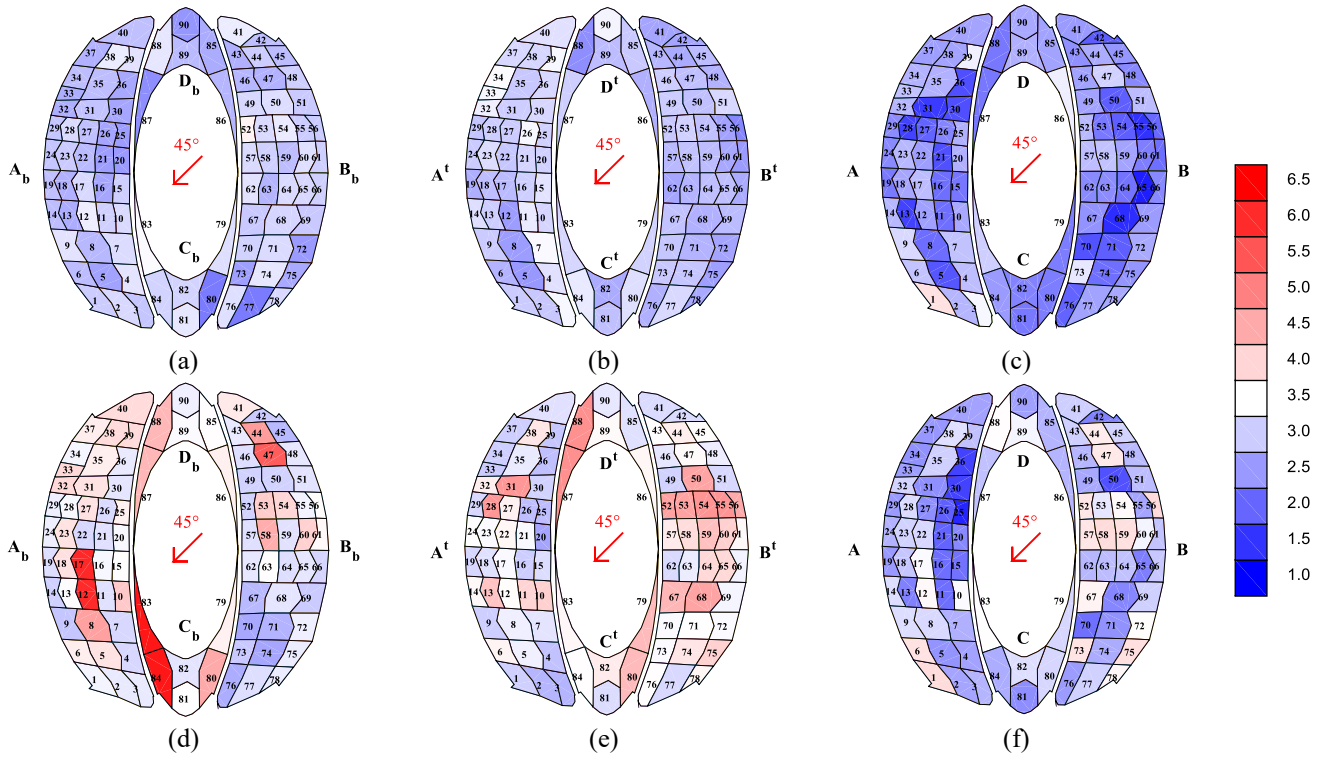

Fig. 14 Peak factors: (a) $g_{,max}$bottom, (b) $g_{,max}$top, (c) $g_{,max}$net, (d) $g_{,min}$bottom, (e) $g_{,min}$top, (f) $g_{,min}$net, θ=45°

Figs. 13 - 15 show the distribution of the peak factors of the face and net pressures for wind angles of 0°, 45° and 90°, respectively; white areas indicate values in the order of 3.5, which is the design value commonly adopted by wind loading codes; blue areas indicate a lower value of the peak factor, whereas red areas indicate a larger value.

First, it is observed that the peak factors of net pressures are generally lower than those of face pressures; this is the effect of the favorable combination of the pressure fluctuations on the top and bottom faces. Then it is

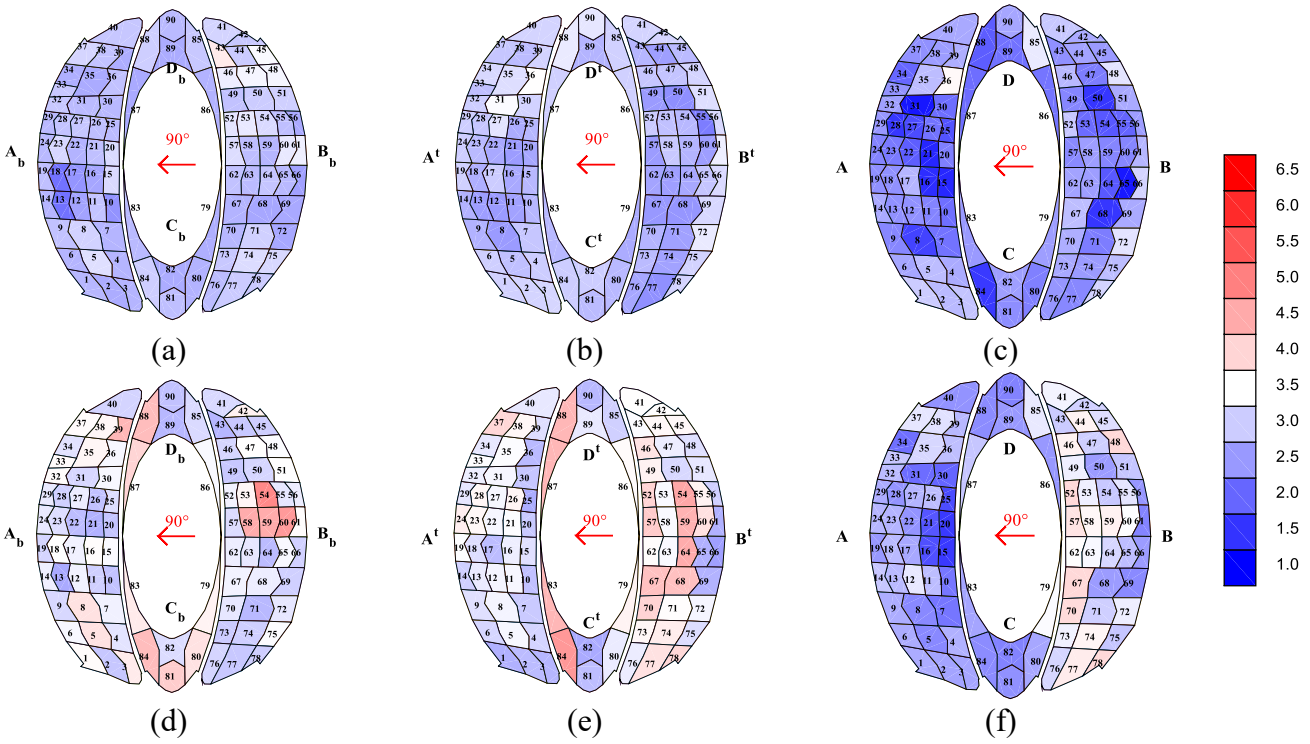

Fig. 15 Peak factors: (a) $g_{,max}$bottom, (b) $g_{,max}$top, (c) $g_{,max}$net, (d) $g_{,min}$bottom, (e) $g_{,min}$top, (f) $g_{,min}$net, θ = 90°

observed that peak factors for the maximum pressures are lower than 3.5, except for a very limited number of exceptions; this indicates that the use of the code value of 3.5 is appropriate and on the safe side. On the other hand, the peak factors for the minimum pressures are diffusely larger than 3.5, and can be as high as 6.0.

For θ=0° (Fig. 13) on the bottom face the peak factors of the maximum pressure are mainly lower than 3.5, but locally they can attain values as high as 6.0; on the top face values lower and higher than 3.5 are almost balanced; as a combination of these, for net pressures only a limited number of areas feature values of the peak factor of maximum pressures larger than 3.5, and never in excess of 4.5. A similar conclusion is found also for θ=45° (Fig. 14).

Finally, for θ=90° (Fig. 15), the peak factors of maximum face pressures are globally smaller than for θ=0° and θ=45°. As an example, Fig. 15(f) shows that in zone B the values range from 2.5 to 4.5, whereas in zone A they are between 1 and 3.5. As to net pressures, the same conclusion found for θ=0° and θ=45° can be drawn, with only a limited number of areas featuring values of the peak factor of maximum net pressures larger than 3.5, and never in excess of 4.5.

6. Combination factors

As shown in Figs. 5, 6 and 7, the net peak pressure coefficients (i.e., maxima and minima) do not coincide with the algebraic difference between peak pressure coefficients on the top and on the bottom of the roof surface. The difference increases when the correlation coefficients between the top and bottom pressure time-series decrease.

For canopy roof with a regular shape, a measure of this effect was given by codes AS-NZS 1170-2 (2011) as combination factors, ranging between 0.8 and 0.9. The combination factor k^+ and k^-, for positive (downward) and negative (upward) net pressures, respectively, are defined in this paper according to Eq. (4).

$$k^+ = \frac{C_{p,max}net}{C_{p,max}top - C_{p,min}bottom}$$
$$k^- = \frac{C_{p,min}net}{C_{p,min}top - C_{p,max}bottom} \quad (4)$$

For the unconventional shape discussed here, the combination factors range between 0.57 and 0.98, as shown by wind tunnel tests results reported in Figs. 16 and 17 for positive (downward) and negative (upward) net pressures of all pressure taps, respectively, and wind angles 0°, 45° and 90°.

It is worth to underline that Fig. 16 and 17 only report combination factors larger than zero, that corresponds to peak actions with the same orientation on the top and bottom surfaces. Only positive values are in fact relevant for design purposes.

In general, it is observed that the combination factors are rather smaller than 1. For a wind angle equal to 0°, the combination factors shown in Figs. 16b and 17b take their largest values (from 0.6 to 1) in small areas in the windward portion of the roof in the case of positive net coefficients, and in the leeward portion of the roof for negative net pressure coefficients.

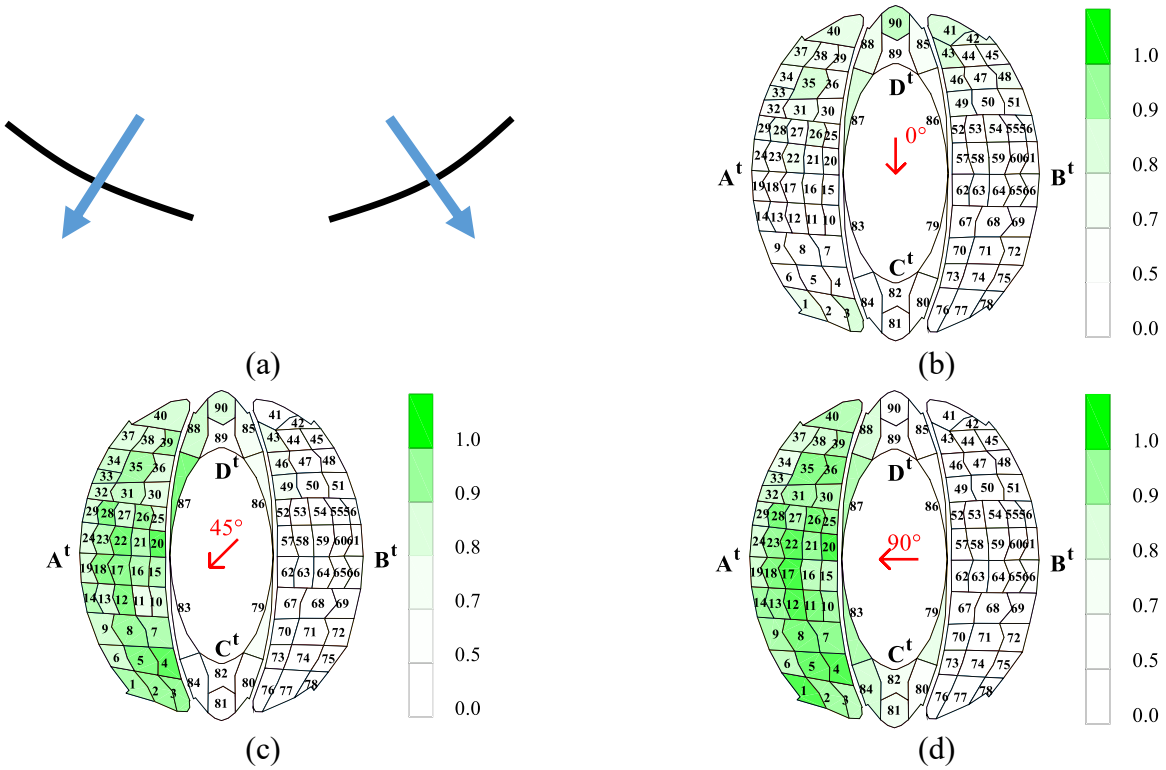

Fig. 16 Combination factors k^+ for positive $C_{p,net}$

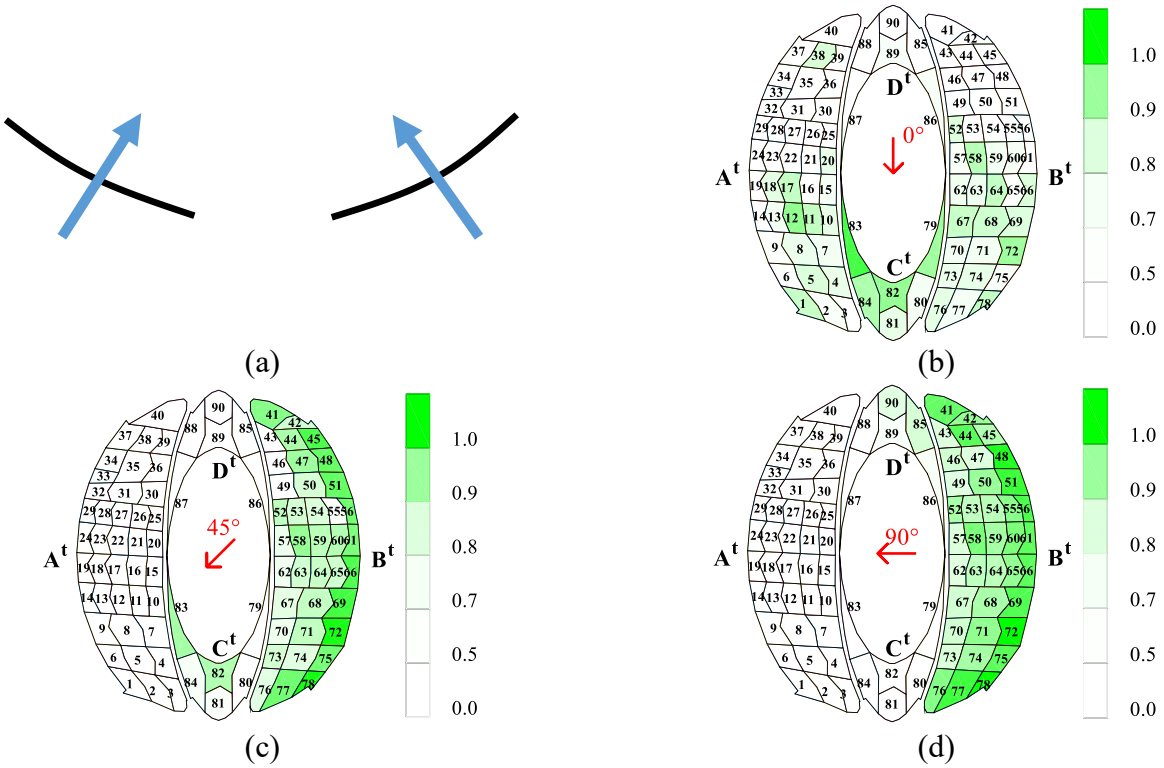

Fig. 17 Combination factors k^- for negative $C_{p,net}$

For wind angles equal to 45° (Figs. 16(c) and 17(c)) and 90° (Figs. 16(d), and 17(d)), the largest combination factors are found on the leeward and windward portions of the roof, when the net pressure coefficients are positive and negative, respectively. According to these results, combination factors for a canopy roof with unconventional shape, prove to be on average significantly smaller than values given by code AS-NZS 1170-2 2011 for simpler geometries.

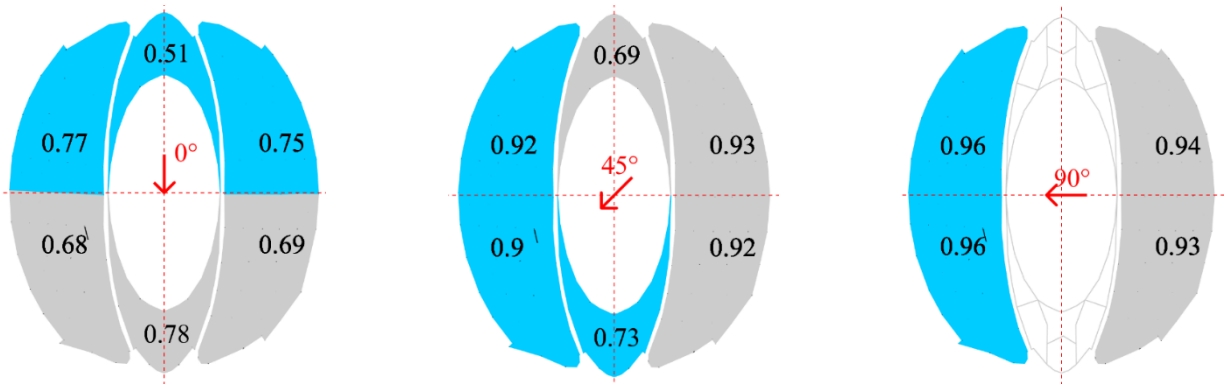

(a) (b) (c)

Fig. 18 Combination factors K+ and K+ for resultant forces on the six subdomains of the roof

Overall combination factors K^+ and K^- were also evaluated for 6 regions in which the roof was divided (Fig. 18), by comparing the extreme values of the resultant net force time-history on each region (positive downward and negative upward) and the difference between the extremes values of the resultant forces on the top and bottom sides

$$K^+ = \frac{\left[\sum_{i=1}^{n}(A_i \cdot C_p(t)net)\right]_{max}}{\left[\sum_{i=1}^{n}(A_i \cdot C_p(t)top)\right]_{max} - \left[\sum_{i=1}^{n}(A_i \cdot C_p(t)bottom)\right]_{min}}$$

$$K^- = \frac{\left[\sum_{i=1}^{n}(A_i \cdot C_p(t)net)\right]_{min}}{\left[\sum_{i=1}^{n}(A_i \cdot C_p(t)top)\right]_{min} - \left[\sum_{i=1}^{n}(A_i \cdot C_p(t)bottom)\right]_{max}} \quad (5)$$

Fig. 18 shows K^+ and K^- for 0°, 45° and 90°. Light blue means resultant forces downward, light gray means resultant forces upward. It is expected that K+ and K- are closer to unity for larger correlations between top and bottom pressures; results reported in Figs. 16 and 17 for local combination factors k+ and k- and in Fig. 18 for region combination factors K+ and K- are therefore in agreement with correlation maps of Fig. 9.

For the case under investigation, the smallest values (i.e. between 0.51 and 0.75) of the combination factor is found for 0°, whereas the largest values (i.e., between 0.93 and 0.96) are found for 90°.

7. Conclusions

Wind tunnel pressure measurements on a large span project canopy roof for the Pescara football stadium in Italy, were carried out. The experiments aimed at investigating the differences between the wind loads on the bottom and on the top faces of the roof, and the way in which these combine to give rise to net loads. The statistics of the pressure coefficients on the two faces of the roof, together with their correlation were discussed for three different wind angles of 0°, 45° and 90°.

In general, it is found the both static and dynamic pressures on the two faces of the roof tend to compensate with each other, giving rise to net loads smaller than what they would be through simple addition of the face pressures. Only in a limited number of cases, the face loads combine in an unfavorable way.

The maps of net mean, maximum and minimum pressure coefficients show that for θ=0° the shape of the roof minimizes the wind action. Contrarily, for θ=90° the roof is loaded with opposite wind actions (i.e. upward and downward) between zones A and B. This is significant from the structural design point of view, as it brings that zones C and D, which are located between zones A and B, can be loaded with opposite loads on a single cable net; this situation can affect the stability of the tensile structure.

Pressure peaks and peak factors were also investigated. It was found that there is a significant portion of the roof, depending on the wind angle, featuring non-Gaussian pressure fluctuations. As an effect of this, peak factors vary significantly. In particular, it was found that the conventional value of the peak factor equal to 3.5 globally tends to overestimate the net wind load. However, when the face pressures are analyzed much larger peak factors than 3.5, are found.

Analysis of the correlation between the pressures acting on the bottom and top faces of the roof proves to be mainly negative, which means that the pressure fluctuations combine in a favorable way and therefore partially cancel with each other. Only limited areas of the roof feature a positive correlation between top and bottom pressures, bringing larger net dynamic loads. Experimental results show that the correlation between pressure coefficients on the top and on the bottom faces is small for most of the roof area. It means that the maximum and minimum values of the net pressure time series cannot be obtained as the algebraic difference between maximum and minimum pressure coefficients on the top and bottom surfaces. To take this effect into account, combination factors similar to those considered in AS-NZS 1170-2 (2011) are therefore introduced, both at the local scale and for six subdomains of the roof.

According to results of this research, combination factors for a canopy roof with unconventional shape are significantly affected by the wind angle of attack. In particular, for some wind directions they are much smaller,

both at the local and global scale, than values given by code AZ-NZS 1170-2 (2011) for simpler geometries.

Acknowledgments

Prof. Piero D'Asdia (University "G. d'Annunzio" of Chieti-Pescara, Italy) is acknowledged for his support and guidance in the testing phase. Dr. Sara Giangreco is also acknowledged for her collaboration to the design of the canopy model and to the experimental campaign. Prof. Michele Barbato of the University of California Davis (USA) is acknowledged for some valuable discussion about non-Gaussian processes.

References

AS-NZS 1170-2 (2011), Structural design actions - Part 2: Wind actions [By Authority of New Zeland Structure Verification Method B1/Vm1].

ASCE (2010a), ASCE 7-10: *Minimum Design Loads for Buildings and Other Structures*. American Society of Civil Engineers (ASCE), Reston, U.S.A.

ASCE (2010b), ASCE/SEI 19-16: *Structural Applications of Steel Cables for Buildings*. American Society of Civil Engineers (ASCE), Reston, U.S.A.

ASCE (2010c), ASCE/SEI 55-10: *Tensile Membrane Structures*. American Society of Civil Engineers (ASCE), Reston, U.S.A.

Barbato, M., Petrini, F., Unnikrishnan, V.U. and Ciampoli, M. (2013), "Performance-based hurricane engineering (PBHE) framework", *Struct. Saf.*, **45**, 24-35. https://doi.org/10.1016/j.strusafe.2013.07.002.

Beccarelli, P. (2015), "Biaxial Testing for Fabrics and Foils Optimizing devices and procedures", Springer International Publishing. Berlin. Germany. https://link.springer.com/book/10.1007%2F978-3-319-02228-4.

Biagini, P., Borri, C. and Facchini, L. (2007), "Wind response of large roofs of stadiums and arena", *J. Wind Eng. Ind. Aerod.*, **95**(9-11), 871-887. https://doi.org/10.1016/j.jweia.2007.01.025.

Birchall, M. (2015), "Recent developments in architectural fabric structures in Europe: The design and construction of the London 2012 Olympic Stadium and its context in the European fabric structures market", *Fabric Struct. Architect.*, 773-817. https://doi.org/10.1016/B978-1-78242-233-4.00022-X.

CEN, 2005. EN 13782: *Temporary Structures-Tent-Safety*. Comité Européen de Normalization (CEN), Brussels (Belgium).

Chilton, J. (2010), "Tensile structures – textiles for architecture and design", *Textiles, Polymers Compos. Build.*, 229-257. https://doi.org/10.1533/9780845699994.2.229.

Ciampoli, M. and Petrini, F. (2012), "Performance-based Aeolian risk assessment and reduction for tall buildings", *Probabilist. Eng. Mech.*, **28**, 75-84. https://doi.org/10.1016/j.probengmech.2011.08.013.

Colliers J., Mollaert M., Degrootec J. and De Laet L. (2019), "Prototyping of thin shell wind tunnel models to facilitate experimental wind load analysis on curved canopy structures", *J. Wind Eng. Ind.* Aerod., **188**, 308-322. https://doi.org/10.1016/j.jweia.2019.03.004.

Cook, N.J. and Mayne, J.R. (1979), "A novel working approach to the assessment of wind loads for equivalent static design", *J. Wind Eng. Ind. Aerod.*, **4**(2), 149-164. https://doi.org/10.1016/0167-6105(79)90043-6.

Cook, N.J. and Mayne, J.R. (1980), "A refined working approach to the assessment of wind loads for equivalent static design", *J. Wind Eng. Ind. Aerod.*, **6**(1-2), 125-137. https://doi.org/10.1016/0167-6105(80)90026-4.

D'Asdia, P., Rizzo, F. and Sepe, V. (2006), "Study of a tension structure shape and of the interaction of wind loads: Pescara stadium roof", *9th National Conference of Wind Engineering*, Pescara, Italy (in Italian).

Davenport, A.G. (1964), "Note on the distribution of the largest value of a random function with application to gust loading", *Proceedings of the Institution of Civil Engineers*, **28**(2), 187-196.

Daw, D.J. and Davenport, A.G. (1989), "Aerodynamic damping and stiffness of a semi-circular roof in turbulent wind", *J. Wind Eng. Ind. Aerod.*, **32**(1-2), 83-92. https://doi.org/10.1016/0167-6105(89)90019-6.

Elashkar, I. and Novak, M. (1983), "Wind tunnel studies of cable roofs", *J. Wind Eng. Ind. Aerod.*, **13**(1-3), 407-419. https://doi.org/10.1016/0167-6105(83)90160-5.

Eswaran M., Verma R.K. and Reddy G.R. (2016). "Wind-induced loads and integrity assessment of hyperboloid reflector of solar power plants", *Alexandria Eng. J.*, **55**(2), 837-850. https://doi.org/10.1016/j.aej.2016.02.005.

Foster, B. and Mollaert, M. (2004), "European design guide for tensile surface structures", *TensiNet*, Brussels, Belgium.

Giaralis, A. and Petrini, F. (2017), "Wind-induced vibration mitigation in tall buildings using the tuned mass-damper-inerter", *J. Struct. Eng. ASCE*, **143**(9), 04017127. https://doi.org/10.1061/(ASCE)ST.1943-541X.0001863.

Ginger, J.D. and Letchford, C.W. (1994), "Wind loads on planar canopy roofs, part 2: fluctuating pressure distributions and correlations", *J. Wind Eng. Ind. Aerod.*, **51**(3), 353-370. https://doi.org/10.1016/0167-6105(94)90068-X.

Holmes, J.D. and Wood, G.S. (2001), "The determination of structural wind loads for the roofs of several venues for the 2000 olympics", *ASCE Structures Congress*, Washington D.C., May.

Huang, M.F., Lou, W., Chan, C.M., Lin, N. and Pan, X. (2013). "Peak distributions and peak factors of wind-induced pressure processes on tall buildings", *J. Eng. Mech.*, **139**(12), 1744-1756. https://doi.org/10.1061/(ASCE)EM.1943-7889.0000616.

Kareem, A. (1997), "Correlation structure of random pressure fields", *J. Wind Eng. Ind. Aerod.*, **69**, 507-516. https://doi.org/10.1016/S0167-6105(97)00181-5.

Kasperski, M. and Niemann, H-J. (1992), "The load-response-correlation method - a general method of estimating unfavourable wind load distributions for linear and nonlinear structural behaviour", *J. Wind Eng. Ind. Aerod.*, **43**(1-3), 1753-1763. https://doi.org/10.1016/0167-6105(92)90588-2.

Ke, S., Yu, W. and Ge, Y. (2018), "Wind load characteristics and action mechanism on internal and external surfaces of super-large cooling towers under wind-rain combined effects", *Mathematica. Problems Eng.*, **2018**, 1-22. https://doi.org/10.1155/2018/2921709.

Kumar, K.S. and Stathopoulos, T., (2000), "Wind loads on low building roofs: a stochastic perspective", *J. Struct. Eng.*, **126**(8), 944-956. https://doi.org/10.1061/(ASCE)0733-9445(2000)126:8(944).

Kwon, D. and Kareem, A. (2011), "Peak factors for non-gaussian load effects revisited", *J. Struct. Eng.*, **137**(12), 1611-1619. https://doi.org/10.1061/(ASCE)ST.1943-541X.0000412.

Lazzari, M, Majowiecki, M, Vitaliani, R.V. and Saetta, A.V. (2001), "Nonlinear F.E. analysis of Montreal olympic stadium roof under natural loading conditions", *Eng. Struct.*, **31**(1), 16-31. https://doi.org/10.1016/j.engstruct.2008.07.010.

Lazzari, M., Saetta, A.V. and Vitaliani, R.V. (2001), "Non-linear dynamic analysis of cable-suspended structures subjected to wind actions", *Comput., Struct.*, **79**(9), 953-969. https://doi.org/10.1016/S0045-7949(00)00187-5.

Letchford, C.W., Row, A., Vitale A. and Wolbers, J. (2000), "Mean wind loads on porous canopy roofs", *J. Wind Eng. Ind. Aerod.*, **84**(2), 197-213. https://doi.org/10.1016/S0167-6105(99)00103-8.

Majowiecki, M. (2004), *Tensostrutture: Progetto e Controllo*. Edizioni Crea, Milan, Italy (in Italian).

Massey, F.J. (1951), "The Kolmogorov-Smirnov test for goodness of fit", *J. Am. Stat. Assoc*., **46**(253), 68-78.

Nakamura, O., Tamura, Y., Miyashita, K. and Itoh, M. (1994), "A case study of wind pressure and wind-induced vibration of a large span open-type roof", *J. Wind Eng. Ind. Aerod.*, **52**, 237-248. https://doi.org/10.1016/0167-6105(94)90050-7.

Natalini, B., Marighetti, J.O. and Natalini, M.B. (2002), "Wind tunnel modelling of mean pressures on planar canopy roof", *J. Wind Eng. Ind. Aerod.*, **90**(4-5), 427-439. https://doi.org/10.1016/S0167-6105(01)00205-7.

Natalini, M.B., Morel, C. and Natalini, B. (2013), "Mean loads on vaulted canopy roofs", *J. Wind Eng. Ind. Aerod.*, **119**, 102-113. https://doi.org/10.1016/j.jweia.2013.05.001.

Rizzo, F., Giangreco, S., D'Asdia, P. and Sepe V. (2005), "Design of a tension structure to cover the Adriatico stadium of Pescara", *XX CTA*, Ischia, Italy, (in Italian).

Rizzo, F. and Sepe, V. (2015), "Static loads to simulate dynamic effects of wind on hyperbolic paraboloid roofs with square plan", *J. Wind Eng. Ind. Aerod.*, **137**, 46-57. https://doi.org/10.1016/j.jweia.2014.11.012.

Rizzo, F. and Ricciardelli, F. (2017), "Design approach of wind load for Hyperbolic paraboloid roof with circular and elliptical plan", *Eng. Struct.*, **139**, 153-169.

Rizzo, F., Barbato, M. and Sepe, V. (2018), "Peak factor statistics of wind effects for hyperbolic paraboloid roofs", *Eng. Struct.*, **173**, 313-330. https://doi.org/10.1016/j.engstruct.2018.06.106.

Sahini, D. (2004), "Wind tunnel blockage corrections: a computational study", Master Thesis, Texas Tech University, Texas, U.S.A.

Takeda, F., Yoshino, T. and Uematsu, Y. (2014), "Design wind force coefficients for hyperbolic paraboloid free roofs", *J. Phys. Sci. Appli.*, **4**(1), 1-19.

Uematsu, Y., Iizumi, E. and Stathopoulos, T. (2007), "Wind force coefficients for designing free-standing canopy roofs", *J. Wind Eng. Ind. Aerod.*, **95**(9-11), 1486-1510. https://doi.org/10.1016/j.jweia.2007.02.015.

Uematsu, Y., Stathopoulos, T. and Iizumi, E. (2008), "Wind loads on free-standing canopy roofs: part 1 local wind pressures", *J. Wind Eng. Ind. Aerod.*, **96**(6-7), 1015-1028. https://doi.org/10.1016/j.jweia.2007.06.047.

Uematsu, Y., Miyamoto Y. and Gavansky, E. (2014), "Wind loading on a hyperbolic paraboloid free roof", *J. Civil Eng. Architect.*, **8**(10), 1233-1242. http://DOI:10.17265/1934-7359/2014.10.004.

Uematsu, Y., Miyamoto, Y. and Gavansky, E. (2015), "Effect of porosity on the wind loads on a hyperbolic paraboloid canopy roof", *J. Civil Eng. Architect.*, **9**(6), 715-726. http://10.17265/1934-7359/2015.06.009.

Vassilopoulou, I. and Gantes, C. J. (2010), "Vibration modes and natural frequencies of saddle form cable nets", *Comput. Struct.*, **88**(1-2), 105-119. https://doi.org/10.1016/j.compstruc.2009.07.002.

Vassilopoulou, I. and Gantes, C.J. (2011), "Nonlinear dynamic behavior of saddle form cable nets under uniform harmonic load", *Eng. Struct.*, **33**(10), 2762-2771. https://doi.org/10.1016/j.engstruct.2011.06.001.

Vassilopoulou, I. and Gantes, C.J. (2012), "Nonlinear dynamic phenomena in a SDOF model of cable net", *Arch. Appl. Mech.*, **82**(10-11), 1689-1703. https://doi.org/10.1007/s00419-012-0660-2.

AD